



This is a repository copy of *Degradation of inverted architecture CH₃NH₃PbI₃-xCl_x perovskite solar cells due to trapped moisture.*

White Rose Research Online URL for this paper:
<http://eprints.whiterose.ac.uk/128250/>

Version: Published Version

Article:

Bracher, C., Freestone, B.G., Mohamad, D.K. et al. (2 more authors) (2018) Degradation of inverted architecture CH₃NH₃PbI₃-xCl_x perovskite solar cells due to trapped moisture. *Energy Science and Engineering*, 6 (1). pp. 35-46.

<https://doi.org/10.1002/ese3.180>

Reuse

This article is distributed under the terms of the Creative Commons Attribution (CC BY) licence. This licence allows you to distribute, remix, tweak, and build upon the work, even commercially, as long as you credit the authors for the original work. More information and the full terms of the licence here:
<https://creativecommons.org/licenses/>

Takedown

If you consider content in White Rose Research Online to be in breach of UK law, please notify us by emailing eprints@whiterose.ac.uk including the URL of the record and the reason for the withdrawal request.



eprints@whiterose.ac.uk
<https://eprints.whiterose.ac.uk/>

RESEARCH ARTICLE

Degradation of inverted architecture $\text{CH}_3\text{NH}_3\text{PbI}_{3-x}\text{Cl}_x$ perovskite solar cells due to trapped moisture

Christopher Bracher, Benjamin G. Freestone , David K. Mohamad, Joel A. Smith & David G. Lidzey

Department of Physics and Astronomy, University of Sheffield, Sheffield, S3 7RH, UK

Keywords

Degradation, Energy efficiency, Perovskite solar cells, photovoltaics

Correspondence

David G. Lidzey, Department of Physics and Astronomy, University of Sheffield, Sheffield S3 7RH, UK.

E-mail: d.g.lidzey@sheffield.ac.uk

Funding Information

Engineering and Physical Sciences Research Council (Grant/Award Number: 'EP/L01551X/1', 'EP/M025020/1').

Received: 4 April 2017; Revised: 17 October 2017; Accepted: 25 October 2017

Energy Science and Engineering 2018;
6(1): 35–46

doi: 10.1002/ese3.180

Introduction

Perovskite solar cells (PSCs) are a promising technology for low-cost photovoltaics. Despite being first realized only 10 years ago [1], PSCs have seen a remarkably rapid rise in power conversion efficiency (PCE), with champion devices now exhibiting efficiencies over 20% [2] – a value that is comparable to crystalline silicon. Notably, PSCs also boast advantages such as being processed from scalable processes such as spray-deposition [3, 4] or blade coating [5], together with band gap-tuning by control over composition [6]. It is known, however, that many perovskite materials have relatively limited operational stability (although new classes of perovskite materials appear much more stable [7]). It is therefore important to understand the degradation mechanisms that limit operational stability to mitigate such effects.

To date, most lifetime measurements on PSCs have been conducted on so-called standard architecture devices, in which electron extraction proceeds through a

Abstract

We explore degradation pathways within encapsulated $\text{CH}_3\text{NH}_3\text{PbI}_{3-x}\text{Cl}_x$ perovskite devices based on the inverted architecture: ITO/PEDOT:PSS/ $\text{CH}_3\text{NH}_3\text{PbI}_{3-x}\text{Cl}_x$ /PC₇₀BM/LiF/Al. Devices were subjected to more than 670 h of continuous illumination approximating AM1.5, with a *Ts80* lifetime of (280 ± 20) hours determined. Devices stored in the dark underwent a similar drop in efficiency over the same time-period. Using external quantum efficiency, time-resolved photoluminescence, X-ray diffraction, scanning electron microscopy and laser beam induced current mapping, we attribute the primary cause of degradation to reactions with residual moisture trapped in the device, resulting in the decomposition of the perovskite.

transparent contact positioned on top of the device substrate, with hole extraction occurring via a reflective top-contact. Here, lifetime studies on PSCs utilizing this architecture have included the perovskite materials $\text{CH}_3\text{NH}_3\text{PbI}_3$ and $\text{CH}_3\text{NH}_3\text{PbI}_{3-x}\text{Cl}_x$. Here, Chauhan et al. have shown that devices incorporating a $\text{CH}_3\text{NH}_3\text{PbI}_{3-x}\text{Cl}_x$ mixed halide perovskite within an FTO/TiO₂/ $\text{CH}_3\text{NH}_3\text{PbI}_{3-x}\text{Cl}_x$ /P3HT/Ag architecture had a *T80* lifetime of approximately 200 h and 1100 h under dark-storage [8]. Guarnera et al. used the same structure, but included an additional Al₂O₃ nanoparticle layer between the perovskite and Spiro-OMeTAD layers [9]. This significantly improved device stability, with a 5% decrease in PCE observed over 350 h. The improvement is attributed to the buffer layer preventing metal atoms migrating into the perovskite layer and increasing current shunt pathways. Recently, Yin et al. demonstrated that $\text{CH}_3\text{NH}_3\text{PbI}_3$ devices incorporating a TiO₂ layer doped with 1% niobium (Nb) retained 89% of their initial PCE after 1200 h [10]. Recent studies have now turned to a

study of the stability of multication perovskite materials. In particular, Saliba *et al.* demonstrated perovskite devices based on the composition $\text{Cs}_5(\text{MA}_{0.17}\text{FA}_{0.83})_{95}\text{Pb}(\text{I}_{0.83}\text{Br}_{0.17})_3$ having remarkably improved stability when held in a nitrogen atmosphere [7]. On illumination, it was found that the PCE decreased by approximately 10% over an initial 250 h period, before then decaying with a half-life of ~ 5000 h. Further studies have now shown that the stability of caesium-based perovskite devices can be improved through the incorporation of potassium; a result ascribed to the increased phase stability of the reduced-volume lead-halide octahedra [11, 12].

We note, however, that relatively few studies have investigated the stability of so-called “inverted architecture” devices. Here, hole extraction occurs through the bottom transparent contact (next to the substrate) with electron extraction occurring via a top reflective contact. Of note, Xie *et al.* performed a 10 h stability test on unencapsulated ITO/PEDOT:PSS/ $\text{CH}_3\text{NH}_3\text{PbI}_3$ /PCBM/PFN-Br/Ag devices in which the devices had either been annealed under vacuum or remained unannealed [13]. It was found that devices that had not been annealed degraded completely within 2 h, whereas annealed devices remained stable. This was attributed to methylammonium chloride within the film absorbing water, enabling the decomposition of the perovskite. Kim *et al.* also observed complete degradation of unencapsulated $\text{CH}_3\text{NH}_3\text{PbI}_3$ devices within 125 h when stored in air, without illumination [5]. A second “shelf-life” study from Kim *et al.* looked at replacing the PEDOT:PSS hole transport layer with the less hygroscopic copper doped nickel oxide (Cu:NiO_x), resulting in improved stability [14]. Here, the PCE of unencapsulated devices with a PEDOT:PSS hole transport layer decreased by 70% over 250 h, whilst those using Cu:NiO_x were reduced by less than 10%. The lower stability of the devices utilizing PEDOT:PSS was speculated to be due to the acidic and hygroscopic nature of the material, resulting in the degradation of the ITO and the perovskite layer.

In this paper, we report a comprehensive study of the operational stability of perovskite solar cells based on the inverted architecture ITO/PEDOT:PSS/ $\text{CH}_3\text{NH}_3\text{PbI}_{3-x}\text{Cl}_x$ /PC₇₀BM/LiF/Al. Devices were subjected to 670 h of continuous illumination with *JV* scans performed every 15 min, whilst being held at open circuit between measurements. Device were also fabricated and stored under dark conditions over a period of 840 h with *JV* scans measured once a week. External quantum efficiency, time resolved photoluminescence, X-ray diffraction, scanning electron microscopy and laser beam induced current mapping have been used to explore the observed degradation mechanisms. We find that following a 160 h burn-in period, devices undergo decay characterized by a (stabilized) T_{s80} lifetime of approximately 280 h. Devices stored under

dark conditions undergo comparable levels of degradation over the same period. Although we cannot rule out additional degradation of the ITO and perovskite due to the acidic nature of the PEDOT:PSS, we speculate that the decomposition of the perovskite is likely to occur via reactions with residual water trapped in the device (most likely within the PEDOT:PSS hole-extraction layer); a process that is likely accompanied by the formation of trap states at the perovskite interface.

Materials and Methods

Perovskite precursor solutions were prepared by mixing PbCl_2 (Sigma-Aldrich, Dorset, UK; 98% pure) and methylammonium iodide (MAI, Ossila Ltd., Sheffield, UK; 99.9% pure) at a ratio of 1.0:2.9 in a N_2 glovebox. Dimethylformamide (DMF, Sigma-Aldrich, 99.8% pure) was added to the mixture to give a total solid content of 660 mg/mL. The solution was left on a hot plate at 70°C overnight to dissolve.

Solar cells were fabricated on glass substrates coated by a prepatterned layer of ITO (Ossila Ltd., 20 Ω/\square). The substrates were first cleaned by sonication in 5% Hellmanex solution, hot DI water, and isopropyl alcohol (IPA) for 5 min each. Between each sonication the substrates were dump rinsed in hot DI water, and were rinsed with IPA and then dried with nitrogen after the final sonication. A (35 ± 2) nm poly(3,4-ethylenedioxythiophene) poly(styrenesulfonate) (PEDOT:PSS, Ossila Ltd.) hole-transport layer was deposited by spin-coating at 5000rpm, and annealed at 125°C for 15 min. The perovskite precursor solution was spin cast in air (relative humidity of (30 ± 2)%) at 4000 rpm from a solution at 70°C onto substrates initially held at 90°C. We note that the ink formulation used here was optimized to work in air, and *does not produce working devices* if the perovskite is instead deposited in a nitrogen-filled glove box. We have purposely explored this material system, as it is in principle compatible with a high-volume air-based manufacture process. The substrate was then annealed in air at 90°C for 90 min to give a (470 ± 20) nm thick $\text{MAPbI}_{3-x}\text{Cl}_x$ perovskite layer. A (150 ± 5) nm thick PC₇₀BM electron-transport layer was then spin cast at 1000 rpm from chlorobenzene (Sigma-Aldrich, 99.95%) at a concentration of 50 mg/ml in a nitrogen filled glove box. A 2 nm LiF electron-transport layer (0.1 Å/s) and a reflective 100 nm Al cathode (1.0 Å/s) were then deposited by thermal evaporation onto the PC₇₀BM at a base pressure of $<10^{-6}$ mbar. Finally, the devices were encapsulated under nitrogen. This was performed by depositing one drop of UV curable epoxy (supplied by Ossila Ltd.) onto the device. A glass slide (C181, Ossila Ltd.) was then placed on the epoxy droplet which the spread across the device surface. The epoxy was then

cured under a UV lamp (MEGA electronics LV202-E 365 nm peak, $P_{\text{output}} = 2.5 \text{ mW/cm}^2$) for 30 min. We have measured the thickness of the cured epoxy layer and find it to be approximately 90 μm . Microscopy measurements performed on such cured epoxy films between glass slides suggest that this film is uniform, homogeneous and devoid of pinholes or gas-bubbles (see Fig. S1). We believe that the thickness of the epoxy film used here is sufficient to absorb the majority of the incident UV radiation used in film curing. For this reason, we do not detect significant perovskite degradation as a direct result of the UV curing stage, although we suspect that some interaction between the uncured epoxy and the device active layer may reduce initial device performance. Once cured we believe that the epoxy protects the device from environmental degradation without causing further degradation in performance.

Devices were characterized under ambient conditions using a Newport 92251A-1000 AM1.5 solar simulator and a Keithley 237 source meter. The output intensity was calibrated to 100 mW/cm^2 using a NREL certified silicon reference cell. An aperture mask was used to define device area to 0.0256 cm^2 . Devices were light-soaked for 20 min and then measured from -1 to 1 V, then 1 to -1 V at a rate of 0.4 V/s. Lifetime data was taken using an Atlas Suntest CPS+ with a 1500 W xenon bulb with IR reducing filters calibrated to 100 mW/cm^2 . Measurements were performed without an aperture mask from -1 to 1 V with a scan rate of 0.1 V/s and devices were held at open circuit between measurements. Further details of the lifetime testing system, including the spectrum of the illumination can be found in reference [15]. External quantum efficiency (EQE) measurements were performed using a tungsten halogen lamp (LOT Oriel LSB117/5), a monochromator, and a Newport 818-UV calibrated silicon photodiode as the reference. Nominally, identical devices were also prepared for dark-storage tests. Here, such samples were wrapped in aluminum foil and placed inside a light-tight container and only removed for *JV* measurements. The humidity and temperature during dark-storage was 32 ± 2 RH% and 18 ± 2 °C respectively.

Time resolved photoluminescence (TRPL) measurements were performed using a 225 μW , 507 nm pulsed laser (2.5 MHz, 4 μs) to excite the sample and a PicoQuant single photon avalanche photodiode to collect the signal. A 550 nm long pass filter was used to prevent laser light from entering the detector. Measurements were performed under dynamic vacuum of at least 10^{-3} mbar.

Laser beam induced current (LBIC) mapping was performed on freshly fabricated and devices that had been aged by exposure to light from the solar simulator. The system comprised a mechanically chopped laser that was passed through a spatial filter before being focused to a spot size of ~ 1 μm onto the sample via a 50x Mitutoyo

infinity-corrected long working distance objective. The sample was mounted on a computer controlled XY-stage, and moved in a sawtooth pattern in steps of 1 μm . Two different diode lasers were separately used to generate photocurrent; a blue 3mW, 405 nm diode laser (power density of 27 W/cm^2) and a 5 mW, 670 nm (40 W/cm^2). Photocurrent was measured using a Stanford Research Systems SR830 lock-in amplifier referenced to the chopped laser. As the $\text{CH}_3\text{NH}_3\text{PbI}_{3-x}\text{Cl}_x$ has an absorption that is a strong function of wavelength, photocurrent imaging at different wavelengths will probe the generation of charge carriers at different distances into the bulk of the film. We can in fact quantify this using the values for the real and imaginary refractive index for $\text{CH}_3\text{NH}_3\text{PbI}_{3-x}\text{Cl}_x$ (see Fig. S4); we calculate that at 405 nm (670 nm) the laser intensity will drop to $1/e$ of its initial value after penetrating a distance of approximately 30 nm (230 nm) into the film. This indicates that the blue laser will mainly generate carriers toward the perovskite-PEDOT:PSS interface, while the red-laser will generate carriers throughout the bulk of the film.

To explore the evolution in perovskite structure as it underwent degradation, X-ray diffraction was performed on unencapsulated control thin-films consisting of ITO/PEDOT/perovskite glass using a Bruker D8 diffractometer (Cu-K α). Scanning electron microscope (SEM) images were also recorded from the same films using a FEI (Inspect F) operating at a beam energy of 2 keV. In all cases, films were explored immediately after deposition, and then after one and two weeks following storage in the dark in dry air (RH 32%). EDS-SEM analysis was performed using an FEI Inspect F50 at 15 keV accelerating voltage with energy dispersive X-ray spectrometer (Oxford Instruments). All point spectral analysis was performed using AZtecEnergy EDS software (Oxford Instruments, Abingdon, UK).

Results and Discussion

In Figure 1, we plot the power conversion efficiency (*PCE*), fill factor (*FF*), short circuit current density (J_{sc}), and open circuit voltage (V_{oc}) of four $\text{CH}_3\text{NH}_3\text{PbI}_{3-x}\text{Cl}_x$ devices as a function of irradiance time. The data represented by lines was recorded using the Atlas system, whilst the data represented by symbols was taken using the calibrated Newport solar simulator (AM1.5, 100 mW/cm^2). All of the data is normalized to its initial value. It is important to note that a spectral mismatch exists between the xenon lamp of the Atlas system and the solar spectrum, and no aperture mask was used when performing measurements, therefore the data is used only to highlight trends, with all *JV* curves presented being taken using the Newport solar simulator.

Over the course of the 670 h test, the average *PCE* of devices decreased by approximately 80%, with the loss

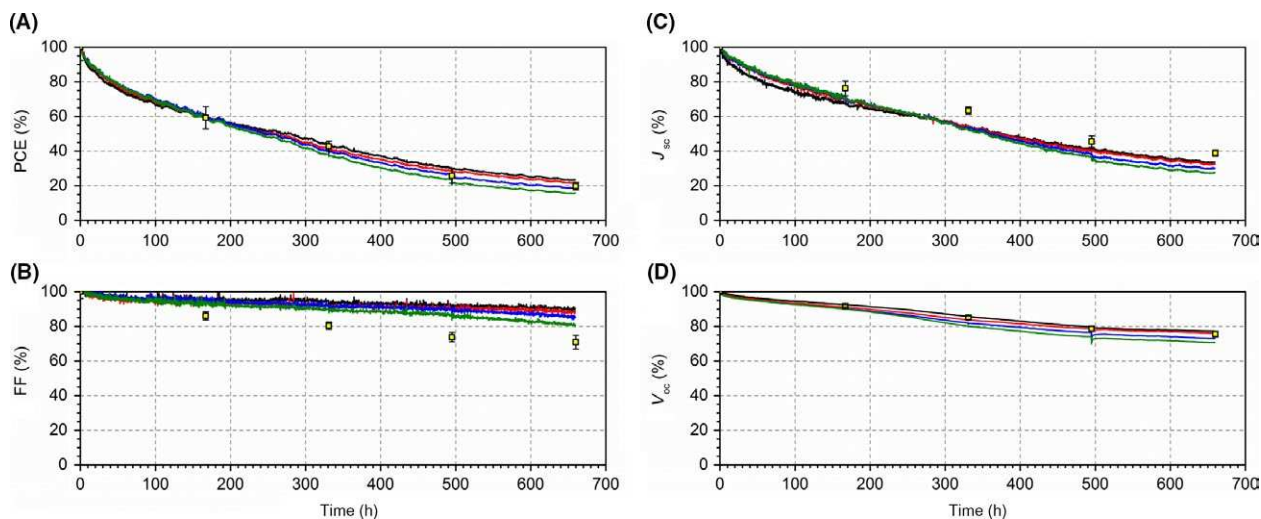


Figure 1. (A) PCE, (B) FF, (C) J_{sc} , and (D) V_{oc} of four $\text{CH}_3\text{NH}_3\text{PbI}_3\text{-xCl}_x$ devices over 670 h of continuous illumination. Solid points are data taken using a calibrated solar simulator. All JV scans were performed from -1 to 1 V.

primarily originating from a $\sim 70\%$ reduction in the J_{sc} . The FF and V_{oc} were affected to a lesser extent, decreasing by 10–20% and 25–30% respectively. The trends seen in the data recorded using the Newport solar simulator are similar to those recorded using the Atlas system, although we observe some difference in the FF recorded using the different systems. We believe that this may originate from the fact that the temperature of the devices recorded using the Atlas system is slightly higher (37 vs. 25°C) [17].

We present the T_{s80} lifetime of the devices held under the solar simulator in Table 1, defined as the time taken to reach 80% of the PCE immediately after the burn-in period (160 h). Data is presented measured using the Atlas Suntest CPS+ system and the calibrated Newport solar simulator. It can be seen that the calculated T_{s80} lifetimes determined by the two systems are in statistical agreement. Our results indicate therefore that the devices have a T_{s80} lifetime of (280 ± 20) hours. This is a shorter lifetime than those seen by Yin et al., who observed 68% loss of PCE after 300 h of aging, followed by very slow degradation over the subsequent 900 h [10]. Further improvements in stability can be gained using cesium-doped FAPbI_3 perovskites [12].

The JV curves used to plot the data-symbols in Figure 1 are plotted in Figure 2A. We also plot the average device

metrics before and after aging in Table 2. It can be seen that we observe a large decrease in the shunt resistance (R_{sh}) [from $1100 \pm 150 \Omega \text{ cm}^2$ to $460 \pm 20 \Omega \text{ cm}^2$], indicative of an increase in leakage pathways, and an increase in the series resistance (R_s), [$5.6 \pm 0.3 \Omega \text{ cm}^2$ to $25 \pm 6 \Omega \text{ cm}^2$], indicative of an increase in the energetic barriers to charge extraction and the creation of trap states within the active layer. Indeed, the decrease in V_{oc} [0.92 ± 0.01 V to 0.69 ± 0.02 V] indicates an increase in charge carrier recombination rate within the device. It can also be observed that there is an increase in the level of hysteresis during the first week of testing (168 h), due to changes in the J_{sc} between forward and reverse scans, further indicating an increase in the density of trap states and the migration of ionic species within the active layer [15–23].

Concomitant with the decrease in J_{sc} , we observe a decrease in the external quantum efficiency (EQE) of the devices as shown in Figure 2B, with the peak EQE value dropping from 80% to 33%. The shape of the EQE curve also changes with time (Fig. S2), with the peak photocurrent wavelength shifting from 468 nm to 432 nm. This is also accompanied by a shift in the band edge (see Fig. S3). The relative loss of EQE at wavelengths greater than 500 nm is characteristic of an increase in the relative levels of PbI_2 within the device [24]. The peak EQE and

Table 1. PCE loss over burn-in period and whole test, and T80 lifetimes calculated using data from both the Atlas Suntest CPS + and the calibrated Newport solar simulator.

Burn-in time (h)	PCE after burn-in (%)	PCE loss over burn-in (%)	PCE loss over 670 h (%)	T_{80} Atlas (h)	T_{80} Newport (h)
160	6.0 ± 0.6	39.0 ± 0.5	78 ± 2	260 ± 10	280 ± 20

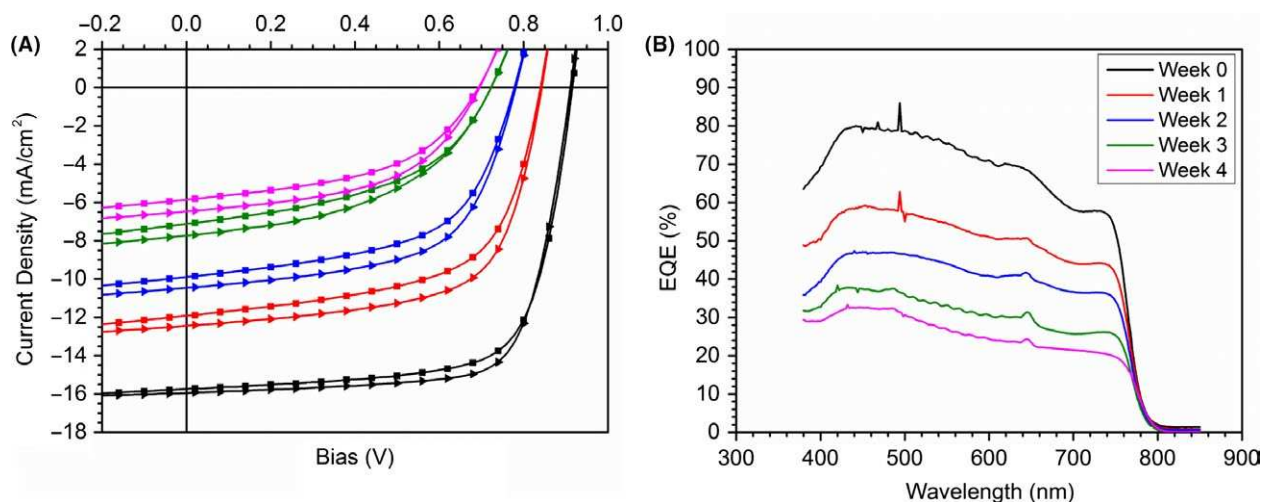


Figure 2. (A) JV curves and (B) EQE measurements for devices at different stages of the lifetime study. Squares in part (A) represent forwards scans, triangles represent backwards scans.

Table 2. Mean device metrics along with their standard deviation for open circuit voltage, short circuit current density, fill factor, power conversion efficiency, and shunt and series resistance, extracted from JV curves, for devices before and after ageing.

Time (h)	Scan direction	PCE (%)	FF (%)	J_{sc} (mA/cm ²)	V_{oc} (V)	Rsh (Ω cm ²)	Rs (Ω cm ²)
0	Forwards	10.2 ± 0.5	70 ± 2	-15.8 ± 0.4	0.92 ± 0.01	1100 ± 150	5.6 ± 0.3
	Backwards	10.6 ± 0.4	73 ± 1	-16.0 ± 0.4	0.91 ± 0.01	1360 ± 350	6.0 ± 0.5
670	Forwards	2.0 ± 0.2	50 ± 3	-6.1 ± 0.3	0.69 ± 0.02	460 ± 20	25 ± 6
	Backwards	2.3 ± 0.4	52 ± 3	-6.7 ± 0.3	0.69 ± 0.02	530 ± 20	23 ± 5

the corresponding wavelengths are detailed in Table S1, along with the integrated and measured J_{sc} .

To further explore the origin of the $\text{CH}_3\text{NH}_3\text{PbI}_{3-x}\text{Cl}_x$ device degradation route, we measured the PCE, FF, J_{sc} and V_{oc} for devices stored under *dark* conditions over a period of 840 h. Figure 3A–D shows average device metrics (normalized to their initial values) determined over 40 individual device pixels. Because our measurements were collected on a weekly basis (to avoid significant exposure to light), we are unable to determine a burn-in time as is done for the data presented in Figure 1. However it is clear that over a time interval of 670 h, the average PCE of the devices has fallen to a value that is around 45% of their original value. This reduction is similar to that observed under exposure to the AM1.5 radiation, which underwent a reduction to around 20% of their original efficiency over the same time period (see Fig. 1A). We note that the reduction in efficiency of dark-stored devices occurs principally as a result of a reduction in V_{oc} and J_{sc} ; a result also in accord with measurements performed under the solar simulator. This reasonably close correspondence between degradation processes observed in dark- and light-storage tests strongly suggests that the dominant degradation mechanism observed here is not catalysed by the exposure to light.

To further explore the mechanisms of the degradation, we have used time resolved photoluminescence (TRPL) measurements to explore carrier recombination dynamics. Here, measurements were performed on encapsulated films based on the structure ITO/PEDOT:PSS/ $\text{CH}_3\text{NH}_3\text{PbI}_{3-x}\text{Cl}_x$ both before illumination, and again after one and two weeks of continuous illumination as shown in Figure 4A. Here, it can be seen that there is an observed drop in the charge carrier lifetime after one week (168 h) of illumination. This effect could result from several different processes, including an increase in the density of trap states within the material, an increase in recombination rate and a decrease charge-carrier mobility [25–27].

We have also performed a preliminary study regarding the effectiveness of the encapsulation system. Images of an unencapsulated and an encapsulated ITO/PEDOT:PSS/ $\text{CH}_3\text{NH}_3\text{PbI}_{3-x}\text{Cl}_x$ film are shown in Figure 4B,C respectively. After 16 h of illumination, it can be seen that the unencapsulated films became yellow; a process characteristic of complete degradation of the $\text{CH}_3\text{NH}_3\text{PbI}_{3-x}\text{Cl}_x$ to PbI_2 in the presence of light [24, 28, 29]. In contrast the encapsulated films retained their original dark-brown color characteristic of $\text{CH}_3\text{NH}_3\text{PbI}_{3-x}\text{Cl}_x$ after two weeks of illumination.

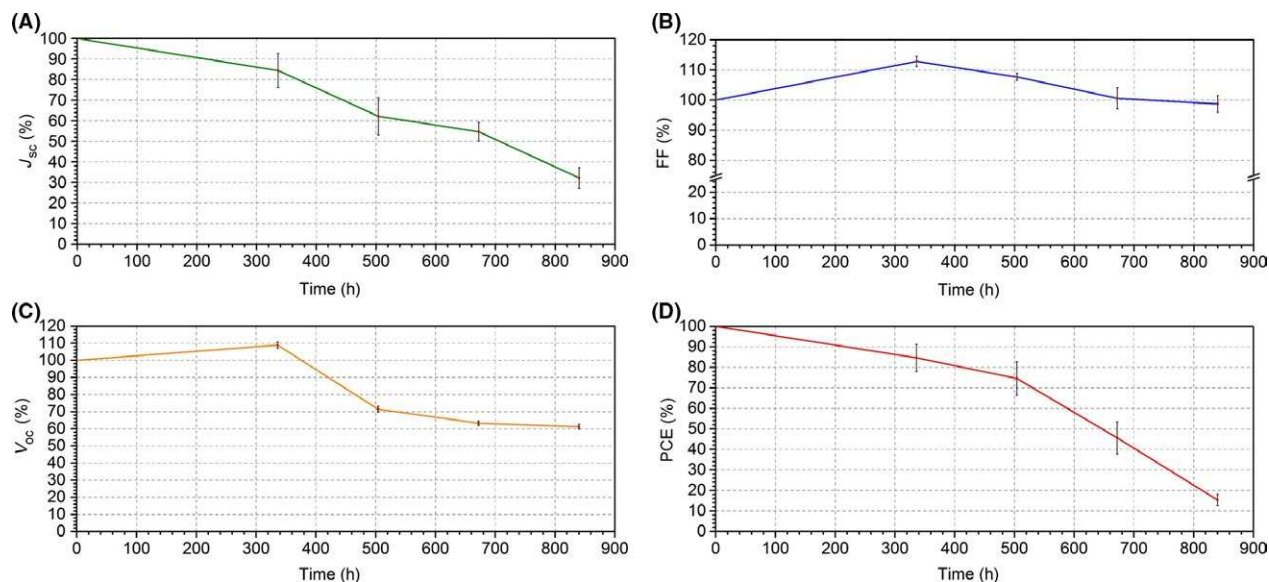


Figure 3. (A) J_{sc} , (B) FF, (C) V_{oc} and (D) PCE of four $\text{CH}_3\text{NH}_3\text{PbI}_{3-x}\text{Cl}_x$ devices over 840 hours of dark-storage. Data points are recorded using a calibrated solar simulator. All JV scans were performed from -1 to 1 V.

To check whether damage to the LiF/Al cathode occurred during the lifetime test, we recorded images of the cathode using an optical microscope both before and after imaging, as shown in Figure 4D,E respectively, however no obvious delamination or formation of pin-holes was observed.

Laser beam induced current mapping was used before and after the irradiation measurements to investigate changes in spatially resolved photocurrent generation, with typical data plotted in Figure 5. Here, Figure 5A,D present optical microscope images recorded from the position corresponding to the LBIC mapping experiments both before and after 670 h of aging under simulated solar irradiation respectively. It can be seen that no obvious degradation of the film is visible. Figure 5B,E were recorded using a 405 nm laser before and after 670 h aging. Figure 5C,F similarly plot data recorded using a 670 nm laser both before and after irradiation respectively. Unfortunately, the location on the device surface of the two sets of measurements is different. We can, however, analyse the photocurrent maps by plotting a histogram of the photocurrent recorded across the device, with all histograms normalized to their peak photocurrent. This is shown in Figure 5G,H for devices imaged at 405 and 670 nm respectively, with each figure plotting histograms for devices both before and after irradiation.

We find that after aging, the average photocurrent signal measured by LBIC (at both imaging wavelengths) reduced by around 60%; a result consistent with the reduction in device J_{sc} measured in aged devices. Note however that this reduction in photocurrent is correlated with a small increase in the standard deviation of the photocurrent

signal, which increased from 4.2% to 7.4%, and 4.0% to 7.2% when imaged at 405 and 670 nm respectively. The relative similarity of the LBIC images recorded from aged devices at 405 and 670 nm suggests that degradation of the perovskite occurs equally both toward the PEDOT:PSS interface and within the bulk of the film. It is apparent, however, that the small increase in the relative width of the photocurrent distribution on aging indicates that perovskite degradation does not occur uniformly across the film, but that some areas are more susceptible to degradation than others. This could be due to thickness or compositional variations of the perovskite film. However, we suspect that this degradation process may be initiated at the edges of the perovskite grains. Larger scale LBIC images covering whole devices were recorded after aging (see Fig. S5). We find that the photocurrent was relatively homogeneous across most pixels, however, an area at the edge of one device exhibited very low current generation, possibly due to complete degradation of the perovskite.

To further characterize the film degradation process, we recorded X-ray diffraction (XRD) spectra on dark-stored samples over a period of 2 weeks to explore the effects of dark-stored degradation. Here, films were not encapsulated, but were stored in a dry environment (at a relative humidity of $\sim 30\%$) to characterize the dominant degradation mechanisms. Typical data are presented in Figure 6, where we show X-ray diffraction around the (110) perovskite and (001) PbI_2 reflections [11, 30–32]. Here, it can be seen that after approximately 2 weeks, the presence of PbI_2 is detected through the growth of a (001) scattering feature at an angle of 12.5° .

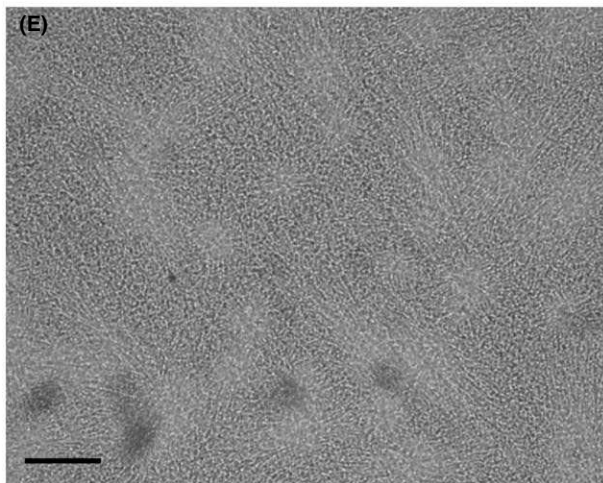
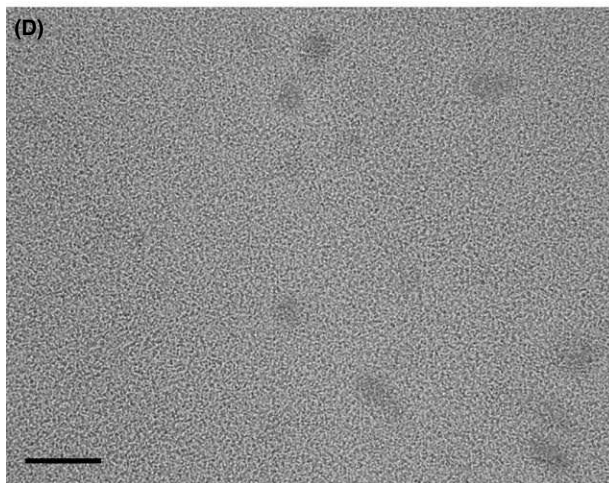
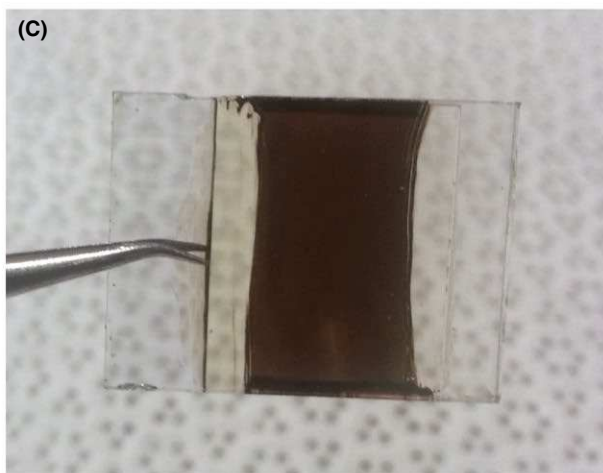
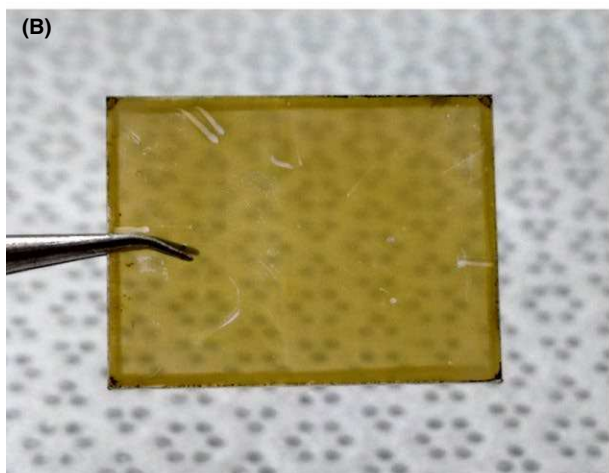
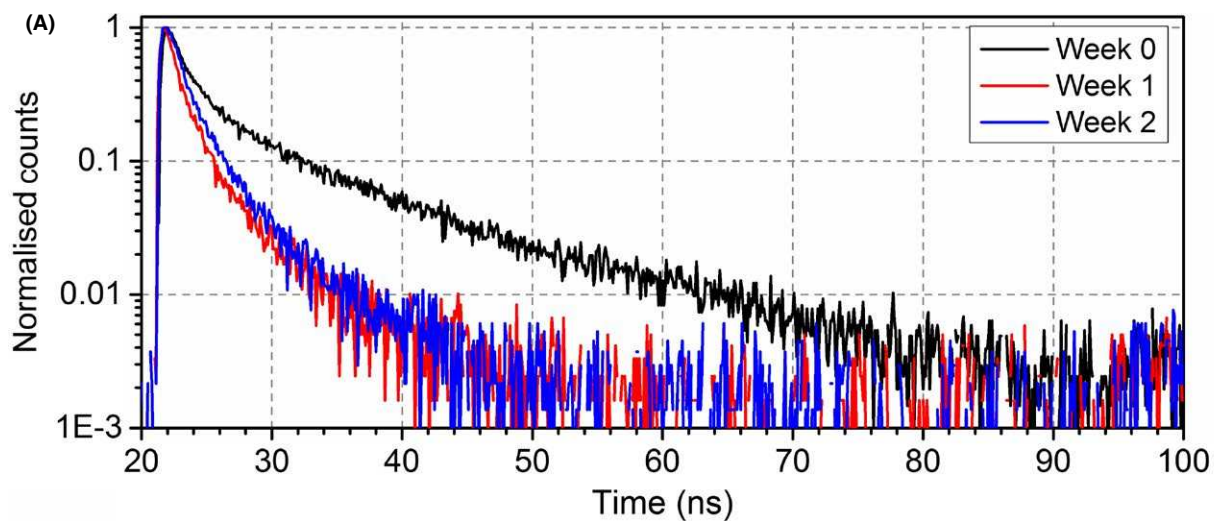


Figure 4. (A) Time resolved photoluminescence data for encapsulated ITO/PEDOT:PSS/CH₃NH₃PbI_{3-x}Cl_x films taken before illumination and after 1 and 2 weeks of continuous illumination. (B) Unencapsulated ITO/PEDOT:PSS/CH₃NH₃PbI_{3-x}Cl_x after 16 h of illumination. (C) Encapsulated ITO/PEDOT:PSS/CH₃NH₃PbI_{3-x}Cl_x after 330 h of illumination. Images (D) and (E) are optical micrographs of the cathode of fresh and aged devices respectively. The scale bar represents 10 μm .

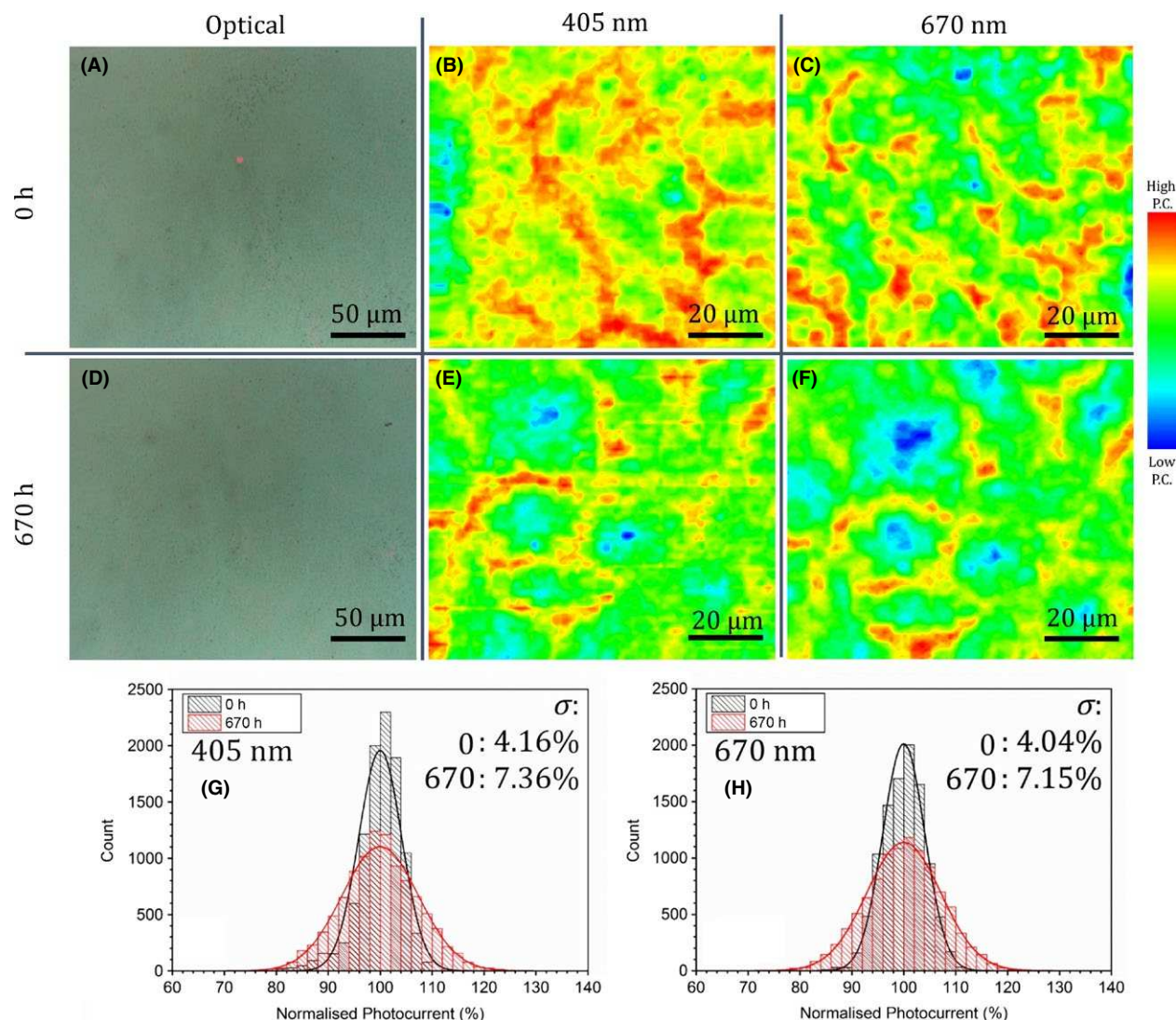


Figure 5. Microscopy of devices before and after 670 h of operation. Parts (A) and (D) show optical microscopy images of the film surface in the regions corresponding to the laser-beam induced current (LBIC) measurements, with images recorded before and after aging respectively. Parts (B) and (E) are LBIC images acquired using a 405 nm laser, before and after aging respectively. Parts (C) and (F), are LBIC images acquired using a 670 nm laser, before and after aging respectively. Parts (G) and (H) are histograms of the data shown in parts (B) and (E), and (C) and (F) respectively. Note that parts (B), (C), (E), and (F) have been independently normalized to the maximum measured photocurrent value.

To explore changes in film morphology at higher spatial-resolution as a result of dark-storage, SEM images were recorded on an unencapsulated ITO/PEDOT:PSS/ $\text{CH}_3\text{NH}_3\text{PbI}_{3-x}\text{Cl}_x$ sample stored in the dark in dry-air for a period of 2 weeks. Figure 7 plots images of the same sample (but recorded at different positions) when freshly cast, and after one and two weeks. Here, images were recorded over a period of 2 weeks. It can be seen from Figure 7C that after 2 weeks, the perovskite grains appear to separate, leaving pin-holes. We propose that such an evolution in film structure is consistent with degradation of perovskite films that commences at grain

boundaries and progresses inwards to the centre of grains. Additionally, Figure S7 is a higher magnification SEM image showing that smaller grains, with a higher proportional grain surface area, are the first to show reduction in size. It is likely that the apparent reduction in perovskite grain size is correlated with the increase in PbI_2 fraction, as evidenced in Figure 6. EDS-SEM analysis was also performed on a degraded perovskite film (Fig. S8). Here, we found that the Pb:I ratio decreased in degraded regions of the film. We found that the Pb:I ratio (atomic wt%) varied from 1:2.98 to 1:1.24 between regions that appeared undegraded to most degraded

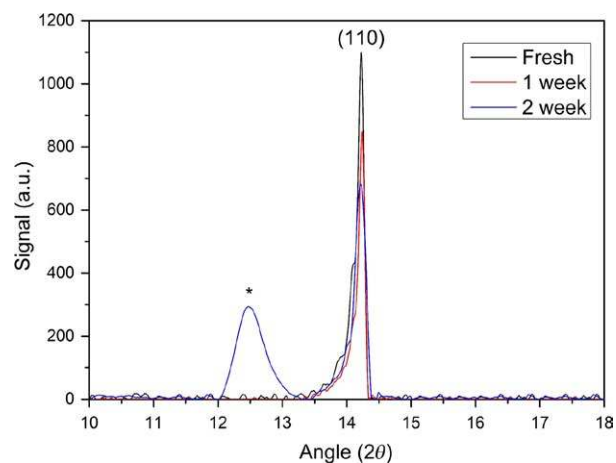


Figure 6. X-ray diffractograms from the same sample imaged across a period of 2 weeks. Note the presence of PbI_2 after 2 weeks under dark-storage, whose scattering peak is identified using a * symbol. See Fig S6 for full angle scan.

respectively. This suggests that in regions where the Pb:I ratio is less than 2, there are also other additional non- PbI_2 degradation products present such as PbCO_3 , Pb(OH)_2 and PbO [33]. The difference could also be due to iodine escaping the film as HI or I_2 degradation products [34].

Our measurements therefore confirm the degradation of the unencapsulated perovskite films under dark-storage, with degraded films appearing less continuous in nature and characterized by an increased fraction of PbI_2 . When the perovskite film is used as the active layer in working devices, we observe a reduction in device performance that also does not appear connected to exposure to light, and thus a light-induced reaction of a superoxide with methylammonium is unlikely to be important here [28, 29]. Rather, the significant decrease in J_{sc} , the reduction in the EQE at wavelengths >500 nm and decrease in charge carrier lifetime suggests a reaction with water resulting in the

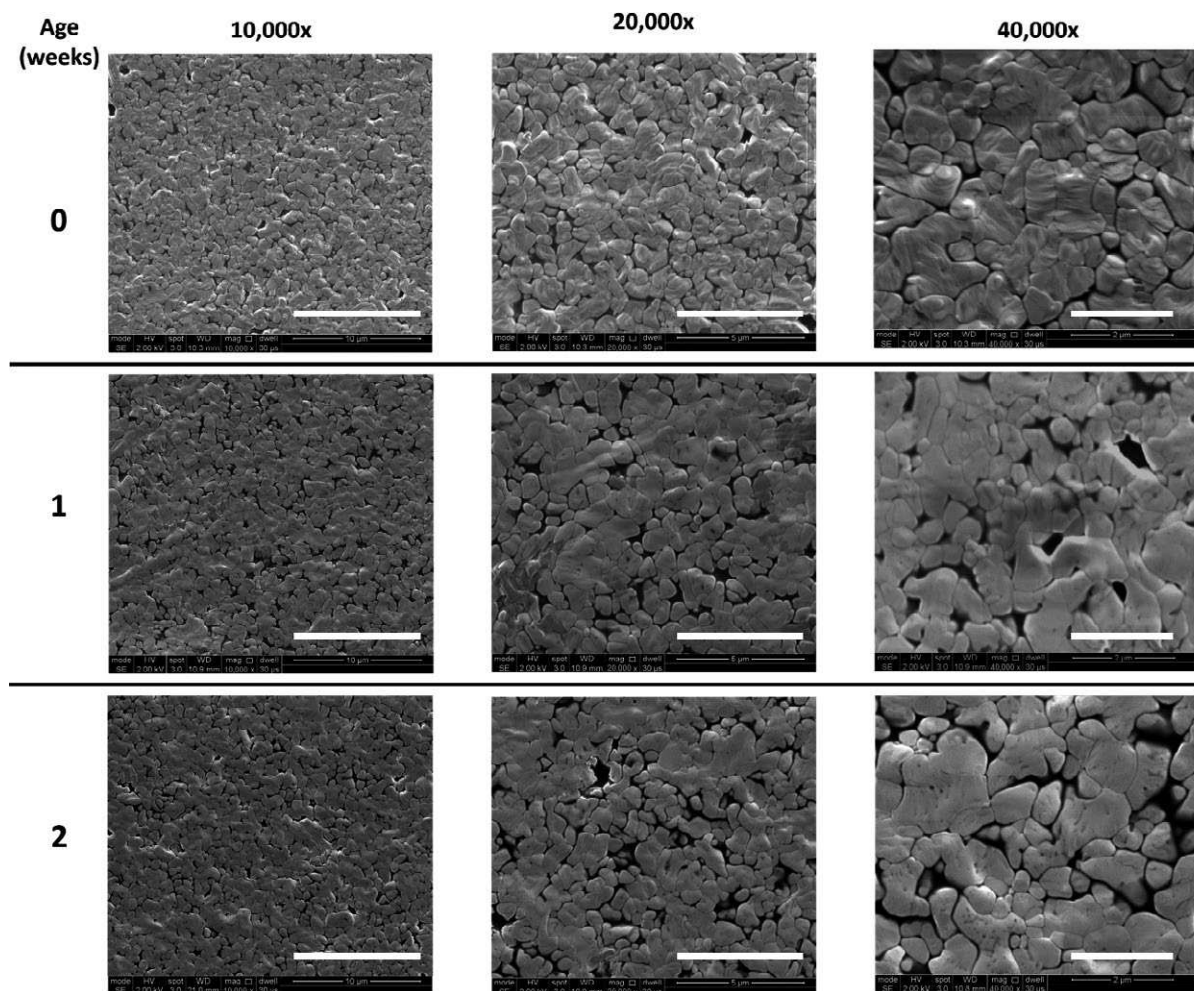


Figure 7. Secondary electron (SE) SEM images of typical regions of perovskite films when freshly prepared, or stored in air (in the dark) for a period of 1 or 2 weeks. Images are presented at 3 different magnifications 10,000 \times , 20,000 \times , and 40,000 \times with the scale bars representing 10, 5, and 2 μm respectively.

decomposition of the perovskite into methylamine (CH_3NH_2), hydroiodic acid (HI), iodine, and PbI_2 [11, 28, 29, 35]. Exact differences in the rate of degradation of light- and dark-stored devices are likely to be explained on the basis of differing temperature. Note however at this stage we cannot fully rule out additional reactions between the acidic PEDOT:PSS and ITO or perovskite resulting in additional degradation pathways [14]. We note however that organic photovoltaics incorporating a PEDOT:PSS/ITO anode retain high efficiency after a period of at least one year [37]. We also speculate that the locally reduced photocurrent observed in the LBIC images of aged devices (see Fig. 5E,F) may correlate with regions of increased PbI_2 concentration. Measurements using LBIC and Raman mapping are planned to test this hypothesis.

We have previously found that polymer:fullerene solar cells (using Ca/Al cathodes) encapsulated in the same manner have operational lifetimes greater than 1 year [36], and thus it is unlikely that the water that catalysed the perovskite degradation entered through the encapsulation. This conclusion is based on the fact that ingress of moisture through the encapsulation would most likely be evidenced through initial degradation toward the edge of the encapsulated film resulting from a diffusion-limited process; a result that was not observed here. We suspect therefore that water that was initially bound in the PEDOT:PSS film (which is known to be highly hygroscopic [37, 38]), underwent diffusion into the perovskite film and initiated its decomposition. However, it is also possible that the air-based process used to deposit the perovskite resulted in a small fraction of water also being trapped within the perovskite layer itself. We note that as methylamine and HI are soluble in water and are volatile, they would normally escape an unencapsulated $\text{CH}_3\text{NH}_3\text{PbI}_{3-x}\text{Cl}_x$ film leaving a PbI_2 film. However, the encapsulation used here is likely to significantly reduce the rate at which these species escape, allowing them to remain in the film. As the highest occupied state of methylamine is located at 1.17 eV above the valence band maximum of the perovskite (and well into the band gap of the material) and the lowest unoccupied state of HI exists ~ 50 meV below the conduction band of the perovskite, both of these species can potentially act as trap-state of sites for nonradiative recombination [39]; a result consistent with the observed increase in charge trapping.

Conclusions

We have explored the operational stability of perovskite solar cells encapsulated using both glass and UV-cured epoxy, based on the inverted architecture structure ITO/PEDOT:PSS/ $\text{CH}_3\text{NH}_3\text{PbI}_{3-x}\text{Cl}_x$ /PC₇₀BM/LiF/Al. We find that when exposed to AM1.5 radiation, the operational lifetime of devices (T_{80} lifetime) is (280 ± 20) hours.

Devices stored under dark conditions had similar decay lifetimes to those exposed to light from the solar simulator. Optical microscopy indicated that this degradation was not apparently connected to observable damage to the LiF/Al cathode. Scanning photocurrent-imaging measurements performed on devices at different excitation wavelengths revealed nonuniformities across the active area of the aged devices, with measurements also confirming that degradation occurred throughout the bulk of the perovskite layer rather than being confined to an interface. Control measurements using XRD on unencapsulated perovskite/PEDOT:PSS films subject to dark-storage in dry air confirmed the generation of PbI_2 through an observed increase in a (001) PbI_2 scattering signal. SEM imaging performed on the same films indicated that degraded films were characterized by less continuous structure. Our measurements suggest therefore that the principle degradation route in the encapsulated devices does not involve an optically induced reaction with a superoxide species. Instead, we speculate that the observed degradation occurred as a result of a reaction between the perovskite and water that was introduced into the device during fabrication (most probably via the hygroscopic PEDOT:PSS hole-extraction layer), facilitating the decomposition of the perovskite into methylamine, hydroiodic acid and PbI_2 . As the escape of methylamine and hydroiodic acid from the device is likely hindered by the device encapsulation, such species may also act as nonradiative recombination centers, reducing charge transport properties and thus reducing device J_{sc} . Our results highlight the importance of removing hygroscopic materials from the device structure.

Acknowledgments

This work was funded by the UK Engineering and Physical Sciences Research Council via research grants EP/M025020/1 “High resolution mapping of performance and degradation mechanisms in printable photovoltaic devices” and EP/J017361/1 “Supersolar Solar Energy Hub”. C.B. thanks the University of Sheffield for a Shine CDT studentship. B.F. and J.A.S. thank The EPSRC New and Sustainable Photovoltaics CDT (EP/L01551X/1) for PhD studentships.

Conflict of Interest

None declared.

References

1. Green, M. A., A. Ho-Baillie, and H. J. Snaith. 2014. The emergence of perovskite solar cells. *Nat. Photonics* 8:506–514.

- Green, M. A., K. Emery, Y. Hishikawa, W. Warta, and E. D. Dunlop. 2016. Solar cell efficiency tables (version 49). *Prog. Photovolt. Res. Appl.* 24:3.
- Barrows, A., A. Pearson, C. Kwak, A. Dunbar, A. Buckley, and D. Lidzey. 2014. Efficient planar heterojunction mixed-halide perovskite solar cells deposited via spray-deposition. *Energy Environ. Sci.* 7:1.
- Mohamad, D.K., J. Griffin, C. Bracher, A.T. Barrows, and D.G. Lidzey. 2016. Spray-cast multilayer organometal perovskite solar cells fabricated in air. *Adv. Energy Mater.* 6:2944–2950.
- Kim, J. H., S. T. Williams, N. Cho, C. C. Chueh, and A. K. Y. Jen. 2015. High-performance and environmentally stable planar heterojunction perovskite solar cells based on a solution-processed copper-doped nickel oxide hole-transporting layer. *Adv. Energy Mater.* 5:2.
- Noh, J. H., S. H. Im, J. H. Heo, T. N. Mandal, and S. Il. 2013. Seok. Chemical management for colorful, efficient, and stable inorganic-organic hybrid nanostructured solar cells. *Nano Lett.* 13:1764–1769.
- Saliba, M., T. Matsui, J.-Y. Seo, K. Domanski, J.-P. Correa-Baena, N. Mohammad Khaja et al. 2016. Cesium-containing triple cation perovskite solar cells: improved stability, reproducibility and high efficiency. *Energy Environ. Sci.* 9:1989.
- Chauhan, A. K., and P. Pankaj. 2017. Degradation in perovskite solar cells stored under different environmental conditions. *J. Phys. D: Appl. Phys.* 50:325105.
- Guarnera, S., A. Abate, W. Zhang, J. M. Foster, G. Richardson, A. Petrozza et al. 2015. Improving the long-term stability of perovskite solar cells with a porous Al₂O₃ buffer layer. *J. Phys. Chem. Lett.* 6:432–437.
- Yin, G., J. Ma, H. Jiang, J. Li, D. Yang, F. Gao et al. 2017. Enhancing efficiency and stability of Perovskite solar cells through Nb-Doping of TiO₂ at low temperature. *ACS Appl. Mater. Interfaces.* 9:10752–10758.
- Nam, J. K., S. U. Chai, W. Cha, Y. J. Choi, W. Kim, M. S. Jung et al. 2017. Potassium incorporation for enhanced performance and stability of fully inorganic cesium lead Halide Perovskite solar cells. *Nano Lett.* 17:2028–2033.
- Li, Z., M. Yang, J. Park et al. 2016. Stabilizing perovskite structures by tuning tolerance factor: formation of formamidinium and cesium lead iodide solid-state alloys. *Chem. Mater.* 28:284–292.
- Xie, F. X., D. Zhang, H. Su, X. Ren, K. S. Wong, M. Grätzel et al. 2015. Vacuum-assisted thermal annealing of CH₃NH₃PbI₃ for highly stable and efficient perovskite solar cells. *ACS Nano* 9:639–646.
- Kim, J. H., P. W. Liang, S. T. Williams, N. Cho, C. C. Chueh, M. S. Glaz et al. 2015. High-performance and environmentally stable planar heterojunction perovskite solar cells based on a solution-processed copper-doped nickel oxide hole-transporting layer. *Adv. Mater.* 27:695–701.
- Bovill, E., N. Scarratt, J. Griffin, H. Yi, A. Iraqi, A. R. Buckley et al. 2015. The role of the hole-extraction layer in determining the operational stability of a polycarbazole:fullerene bulk-heterojunction photovoltaic device. *Appl. Phys. Lett.* 106:73301.
- Lin, Q., A. Armin, R. Chandra, R. Nagiri, P. L. Burn, and P. Meredith. 2014. Electro-optics of perovskite solar cells. *Nat. Photonics* 9:106–112.
- Ono, L. K., S. R. Raga, S. Wang, Y. Kato, and Y. Qi. 2015. Temperature-dependent hysteresis effects in perovskite-based solar cells. *J. Mater. Chem. A* 3:9074.
- Snaith, H. J., A. Abate, J. M. Ball, G. E. Eperon, T. Leijtens, N. K. Noel et al. 2014. Anomalous hysteresis in perovskite solar cells. *J. Phys. Chem. Lett.* 5:1511–1515.
- Shao, Y., Z. Xiao, C. Bi, Y. Yuan, and J. Huang. 2014. Origin and elimination of photocurrent hysteresis by fullerene passivation in CH₃NH₃PbI₃ planar heterojunction solar cells. *Nat. Commun.* 5:5784.
- Zhao, Y., C. Liang, H. Zhang, D. Li, D. Tian, G. Li et al. 2015. Anomalously large interface charge in polarity-switchable photovoltaic devices: an indication of mobile ions in organic–inorganic halide perovskites. *Energy Environ. Sci.* 8:1256.
- Tress, W., N. Marinova, T. Moehl, S. M. Zakeeruddin, N. Mohammad Khaja, M. Grätzel et al. 2015. Understanding the rate-dependent *J*–*V* hysteresis, slow time component, and aging in CH₃NH₃PbI₃ perovskite solar cells: the role of a compensated electric field. *Energy Environ. Sci.* 8:995.
- Zhang, H., C. Liang, Y. Zhao, M. Sun, H. Liu, J. Liang et al. 2015. Dynamic interface charge governing the current–voltage hysteresis in perovskite solar cells. *Phys. Chem. Chem. Phys.* 17:9613.
- Calado, P., A. M. Telford, D. Bryant, X. Li, J. Nelson, B. C. O'Regan et al. 2016. Evidence for ion migration in hybrid perovskite solar cells with minimal hysteresis. *Nat. Commun.* 7:13831.
- Ito, S., S. Tanaka, K. Manabe, and H. Nishino. 2014. Effects of surface blocking layer of Sb₂S₃ on nanocrystalline TiO₂ for CH₃NH₃PbI₃ perovskite solar cells. *J. Phys. Chem. C* 118:16995.
- Chen, Q., H. P. Zhou, T. B. Song, S. Luo, Z. R. Hong, H. S. Duan et al. 2014. Controllable self-induced passivation of hybrid lead iodide perovskites toward high performance solar cells. *Nano Lett.* 14:4158–4163.
- Gunawan, O., T. K. Todorov, and D. B. Mitzi. 2010. Band tailing and efficiency limitation in kesterite solar cells. *Appl. Phys. Lett.* 97:233506.
- Ponseca, C. S., T. J. Savenije, M. Abdellah, K. Zheng, A. Yartsev, T. Pascher et al. 2014. Organometal halide

- perovskite solar cell materials rationalized: ultrafast charge generation, high and microsecond-long balanced mobilities, and slow recombination. *J. Am. Chem. Soc.* 136:5189–5192.
28. Aristidou, N., I. Sanchez-Molina, T. Chotchuangchuchaval, M. Brown, L. Martinez, T. Rath *et al.* 2015. The role of oxygen in the degradation of methylammonium lead trihalide perovskite photoactive layers. *Angew. Chemie - Int. Ed.* 54:8208–8212.
29. Bryant, D., N. Aristidou, S. Pont, I. Sanchez-Molina, T. Chotchuangchuchaval, S. Wheeler *et al.* 2016. Light and oxygen induced degradation limits the operational stability of methylammonium lead triiodide perovskite solar cells. *Energy Environ. Sci.* 9:1655–1660.
30. Burschka, J., N. Pellet, S. J. Moon, R. Humphry-Baker, P. Gao, M. K. Nazeeruddin *et al.* 2013. Sequential deposition as a route to high-performance perovskite-sensitized solar cells. *Nature* 499:316–319.
31. Mohamad, D. K., B. G. Freestone, R. Masters, M. Reinhardt, S. Canning, C. Rodenburg *et al.* 2017. *J. Mater. Chem. C* 5:2352–2359.
32. Dualeh, A., N. Tétreault, T. Moehl, P. Gao, M. K. Nazeeruddin, and M. Grätzel. 2014. Effect of annealing temperature on film morphology of organic–inorganic hybrid perovskite solid-state solar cells. *Adv. Func. Mat.* 24:3250–3258.
33. Huang, W., J. S. Manser, P. V. Kamat, and S. Ptasinska. 2016. *Chem. Mater.* 28:303–311.
34. Delugas, P., A. Filippetti, and A. Mattoni. 2015. *Phys. Rev. B - Condens. Matter Mater. Phys.* 92:1.
35. Frost, J. M., K. T. Butler, F. Brivio, C. H. Hendon, M. Van Schilfhaarde, and A. Walsh. 2014. Atomistic origins of high-performance in hybrid halide perovskite solar cells. *Nano Lett.* 14:2584–2590.
36. Pearson, A. J., G. E. Eperon, P. E. Hopkinson, S. N. Habisreutinger, J. T. W. Wang, H. J. Snaith *et al.* 2016. Oxygen degradation in mesoporous $\text{Al}_2\text{O}_3/\text{CH}_3\text{NH}_3\text{PbI}_{3-x}\text{Cl}_x$ perovskite solar cells: kinetics and mechanisms. *Adv. Energy Mater.* 6:1.
37. Zhang, Y., E. Bovill, J. Kingsley, A. R. Buckley, H. Yi, A. Iraqi *et al.* 2016. *Sci. Rep.* 6:21632.
38. Frost, J. M., K. T. Butler, F. Brivio, C. H. Hendon, M. van Schilfhaarde, and A. Walsh. 2014. Atomistic origins of high-performance in hybrid halide perovskite solar cells. *Nano Lett.* 14:2584–2590.
39. Elschner, A., S. Kirchmeyer, W. Lovenich, U. Merker, and K. Reuter. 2010. *PEDOT: Principles and Applications of an Intrinsically Conductive Polymer.* CRC Press, Boca Raton, FL.

Supporting Information

Additional supporting information may be found in the online version of this article:

Figure S1. 10x optical microscope image of cured epoxy encapsulation between two clean glass slides.

Figure S2. EQE data normalized to the peak value each week, highlighting the relative change in shape and loss of EQE.

Figure S3. Tauc plot of EQE band edge. Inset are the estimated values for the optical bandgap for each week at wavelengths longer than 500 nm

Figure S4. Real and imaginary refractive index for $\text{CH}_3\text{NH}_3\text{PbI}_{3-x}\text{Cl}_x$ as measured by ellipsometry.

Figure S5. Laser beam inducted current maps of all four devices after the 670 h stability test, taken using a 405 nm laser and normalized to the peak photocurrent.

Figure S6. XRD measurements taken on the same sample across 2 weeks of dark-storage.

Figure S7. Secondary electron SEM image showing grains that appear to be decreasing in size when compared to those in Fig. 7 (main text).

Figure S8. EDS-SEM analysis of a degraded sample, (a) SEM image showing three locations for EDS spectral analysis, (b) spectrum at degraded point of film, (c) spectrum at pristine portion of film, (d) spectrum at partially degraded section of film. Quantitative analysis shows the degraded area is lead-rich, with Pb:I ratio (atomic wt%) of 1.24, 2.98, and 2.74 for each spectra (b)–(d).

Table S1. Peak EQE and integrated J_{sc} taken each week during the lifetime study.